

# Turbofan Broadband Noise Prediction using the Lattice Boltzmann Method

D. Casalino\* A. Hazir†

*Exa GmbH, Curiestrasse 4, Stuttgart, 70563, Germany*

A. Mann‡

*Exa Corp., 150 North Hill Drive, Brisbane, 94005, California*

The present work describes a numerical reproduction of the 22-in source diagnostic test (SDT) fan rig of the NASA Glenn Research Center. Numerical flow simulations are performed for three different rotor/stator configurations and one rotational speed, representative of an approach operating condition, by using the lattice-Boltzmann solver PowerFLOW. The full stage and nacelle geometries are considered and results are compared with available measurements. Tripping the rotor blades is shown to lead to a more accurate noise prediction as a consequence of a more accurate prediction of the velocity fluctuation levels in the rotor wake over the whole blade span. Fourier circumferential analyses are performed for an intake and a bypass duct section with the intent of showing the importance of the coupling mechanisms between the blade aerodynamic loading and the duct modal content in the presence of swirling flow and acoustic scattering on the rotor and stator blades. Finally, the effects of adding an acoustic treatment in the intake is shown by directly resolving the unsteady flow field in a one degree of freedom honeycomb layer.

## I. Introduction

MODERN turbofan architectures with very-high bypass ratios provide improved engine performances at lower primary jet exhaust velocities. Higher bypass ratios result in both lower fan rotational and primary jet exhaust velocities, but, due to the different velocity scaling laws, this typically leads to a certain increase of the fan/jet noise ratio in approach conditions. Lower fan tip speed, reduced number of fan blades compensated by increased blade chord, and optimal selection of the rotor/stator blade count typically result in a relative increase between the broadband/tonal noise ratio. The only factor introducing an opposite trend is the reduced nacelle surface available for liners, which are typically tuned to tonal components at blade passage frequencies<sup>a</sup>. As a consequence of the trade-off between jet and fan noise contributions for different engine architectures, and the trade-off between tonal and broadband fan noise contributions for different fan/Outlet Guide Vane (OGV) stage designs, including the effect of liner absorption over a broad frequency range, it is crucial to introduce engine noise prediction methods in the engine design cycles as early and as accurate as possible. Moreover, for under wing engine architectures, the jet/fan noise trade-off should take into account the engine installation effects due to the jet/flap interaction in approach/landing conditions.

State-of-the-art prediction methods used by industry, for jet and fan noise prediction, are mainly based on semi-empirical or semi-analytical formulations, based on noise source statistics derived from Reynolds-Averaged Navier-Stokes (RANS) computations and transposed to far-field noise statistics through suitable propagation models that take into account, at various degrees of approximation, the near-field diffraction and refraction effects. Such a methodology, which is based on a multitude of prediction methods, each one

\*Technical Director, Aerospace.

†Senior Application Engineer, Aerospace.

‡Principal Engineer, Acoustics.

<sup>a</sup>The reduced surface  $S$  is a consequence of the reduced axial extension  $l$  of the nacelle for a constant weight  $W$  and a higher diameter  $D$  ( $S \propto lD \propto W/D$ )

for one specific source model and with its limitations and approximations, result in an additional layer of uncertainty due to the practical difficulty to manage the whole engine design space in a multi-disciplinary framework. The use of high-fidelity numerical simulations able to tackle aerodynamic, aeroacoustic and thermal design aspects in a homogeneous simulation environment, which relies on one engine CAD model, one CFD software, and one or few computational setups specific to the different disciplines, is certainly the long-term solution for turbofan engine design. The goal of the present paper is to measure the fidelity of a hybrid Lattice-Boltzmann/Very Large Eddy Simulation (LB/VLES) flow model<sup>1,2,3,4</sup> in predicting the absolute and relative broadband noise levels generated by a set of realistic fan/OGV configurations, and to demonstrate that accurate predictions can be already achieved in turnaround times that are compatible with industrial time constraints.

Fan broadband noise predictions are currently performed through analytical formulations, based on the combined use of gust/cascade aerodynamic response models<sup>5,6</sup> and infinite duct acoustic models,<sup>7,8,9,10</sup> eventually taking into account some acoustic diffraction and swirl-flow refraction effects, such as the rotor shielding<sup>11</sup> and the acoustic mode trapping between rotor and intake,<sup>12</sup> rotor and stator,<sup>13</sup> and stator and exhaust.<sup>14</sup> The three-dimensional properties of the rotor wake are taken into account through specific axisymmetric empirical turbulence models and use of blade strip approach,<sup>10</sup> or computed from radial profiles of statistical quantities extracted from RANS solutions.<sup>15</sup> The blade twist, sweep and lean are taken into account by the cascade aerodynamic response model, but each blade section is approximated as a flat plate. The blade thickness and camber do not significantly affect the broadband noise levels, which result from a random wake/blade interaction process. Instead, modeling the real shape of the OGV blades is considered to be necessary for an accurate prediction of tonal noise, since this depends on the interference between the waves generated by the periodic interaction between the rotor wakes and the OGV vanes, and thus on the accurate representation of the blade loading signature induced by the wake impingement. In spite of their elegance, there exists a certain conviction that these methods may not provide the correct trends for design variations around reference configurations, without a specific validation and calibration. Moreover, the effect of nonaxisymmetric geometrical elements, like scarfed intakes and pylons in the bypass duct, cannot be taken into account without an additional layer of sophistication, and thus with additional uncertainties and computational costs.

The present analysis follows previous one based on the same LB/VLES technology, but different fan/OGV configurations. Mann *et al*<sup>16</sup> used the Advance Noise Control Fan (ANCF) configuration of the NASA Glenn Research Center<sup>17</sup> to validate broadband and tonal noise prediction capabilities of PowerFLOW, with emphasis on the prediction of the modal duct content. Péro<sup>t et al</sup><sup>18</sup> used the same ANCF model to investigate the effect of a nacelle yaw angle on the radiated acoustic field and on the duct modal content. Casalino *et al*<sup>19</sup> assessed the feasibility of a comprehensive fan/jet turbofan aeroacoustic simulation using a new LB formulation that covers the whole subsonic flow regime ( $M \lesssim 0.95$ ). The ANCF simulation was also repeated and provided very similar tonal and broadband noise levels. An overestimation of the overall noise levels up to about 5 dB and 3 dB in the forward and aft radiation arc, respectively, was reported. Very recently, a new PowerFLOW simulation campaign has been carried out for the ANCF configuration<sup>20</sup> in order to better investigate the effect of some uncertainties in the experiments and in the simulations. The main conclusions of all these studies are the following: (i) the rotating microphone rake used in the ANCF experiment affects the duct modal content, (ii) the CAD model used to build the computational mesh does not account for some details present in the test rig, (iii) the presence of an Inflow Control Device (ICD) in the experiments and not in the simulations may have a non negligible effect on the ingested flow and on the forward far-field noise levels, (iv) the absence of the tip gap in the simulation results in a more coherent rotor wake in the tip region, with a consequent overestimation of the periodic stator excitation. It is a common opinion that the experimental data of the 22-in SDT fan rig of the NASA Glenn Research Center,<sup>21,22</sup> available in the framework of the AIAA Fan Broadband Noise (FBN) prediction workshop, are affected by smaller uncertainties than the ANCF data. Furthermore, the SDT configuration is more suitable for the validation of broadband noise prediction tools. The present effort, therefore, has the main intent to better qualify the accuracy of a fan/OGV broadband noise prediction based on the last PowerFLOW release and the current version of the turbofan noise best practice simulation template.

In a previous work<sup>19</sup> we showed how an acoustic treatment in the intake can be modeled by using an equivalent acoustic porous medium<sup>23</sup> tuned to a certain target frequency/impedance law. A bulk ceramic liner was used as a proof of concept, and results of tonal noise radiation from an axisymmetric intake were shown to be in favorable agreement with frequency-domain finite element solutions of a wave equation for

the acoustic potential in a non-uniform rotational base flow. As an alternative to liner modeling through an equivalent porous medium, which is not straightforwardly defined for a honeycomb liner due to the Helmholtz-resonance mechanism, Mann *et al*<sup>24</sup> have evaluated the mesh resolution required to achieve reliable LB-VLES predictions of the absorption of a one degree of freedom (1-DoF) honeycomb liner constituted of hundreds of cells and orifices. Following that pioneering work, a 1-DoF zero-splice honeycomb liner of realistic porosity and orifice diameter and specifically designed for the SDT tonal noise content, is applied to the present SDT configuration and results for an acoustically treated intake are also reported.

The paper is organized as follows. Information about the geometrical configurations and the computational setup are reported in Section II. In Section III we compare measured and predicted velocity fluctuations on an interstage plane section. Far-field noise results are presented in Section IV, together with the equivalent source power level. Results of an azimuthal Fourier analysis are reported in Section V. Finally, results for an acoustically treated intake and direct simulation of a 1-DoF honeycomb liner are reported in Section VI and compared to corresponding results for an untreated intake. The main findings of the present analyses are summarized in the conclusion section.

## II. Turbofan configuration and computational setup

### II.A. Turbofan geometries

Fig. 1 illustrates the SDT turbofan nacelle. The geometry is perfectly axisymmetric. In order to reproduce the stinger employed in the experiment, a cylindrical prolongation of the centerbody has been added to the CAD model provided by NASA. The rotor radius is 0.2786 m, the bypass exhaust radius is 0.2710 m and the lip intake radius is 0.2962 m. The origin of the reference system used throughout is located in the midpoint of the rotor. The intake lip and bypass exhaust sections are located at  $x = 0.3305$  m and  $x = 0.5587$  m, respectively. Interstage hot-wire measurements have been performed by NASA in the plane  $x = 0.1016$  m, referred to as *station #1*. The rotor is constituted of 22 blades, and the casing/blade-tip gap is about 0.5 m. The location of the junction between the rotating spinner and the centerbody is at  $x = 0.0424$  m. A detailed view of the 1-DoF honeycomb liner is also shown. For visualization purposes, a portion of the perforated face sheet and honeycombs have been removed.

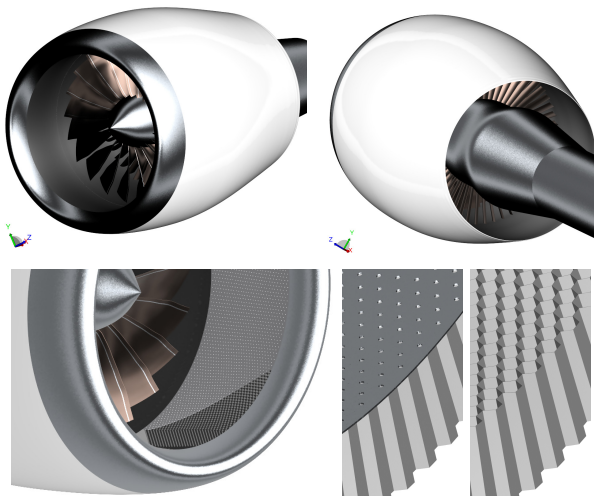


Figure 1. Turbofan SDT baseline configuration: nacelle and details of the liner package.

Fig. 2 shows three variants of the OGV configurations: a 54-vane *baseline* radial OGV, a 26-vane *low-noise* swept OGV and a 26-vane *low-count* radial OGV. All the other parts are them same for the three configurations.

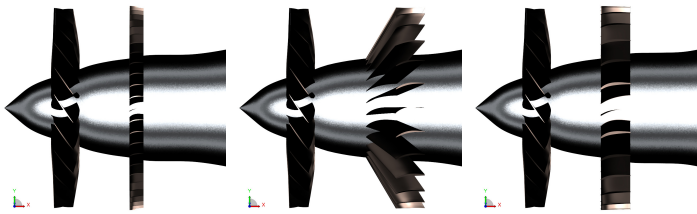


Figure 2. Turbofan SDT configurations: baseline (left), low-noise (middle), and low-count (right).

## II.B. Operating conditions

Among five values of the rotational speed tested by NASA, we consider in this work the one corresponding to the *approach condition*, say  $\Omega = 817.652 \text{ rad/sec}$  (7808 RPM). This corresponds to a rotational tip Mach number of 0.6693 and a Blade Passage Frequency (BPF) of 2862.93 Hz. The ambient conditions are set to a temperature of 288.15 K and a pressure of 101325 Pa. The engine operates at zero incidence in a free-stream of Mach number 0.1.

## II.C. Computational setup and mesh resolution effects

A sketch of the computational setup is shown in Fig. 3. The intake of the nacelle hosts a liner package that can be activated or deactivated. The rotor (red) and the spinner (orange) are encompassed by a volume (purple) that defines the rotating mesh region. The center body (dark gray) is extended with a solid cylinder (light gray). As in the experiments, no primary jet is included in the simulation. The points (red) in the interstage denote the axial location of station #1. The Ffowks-Williams and Hawkings (FW-H) integration surface (green) used to compute the acoustic far-field consists of three parts: a spherical sector around the intake, a cylindrical connector and a conical surface in the exhaust region. The cone is opened at its downstream extremity in order to avoid contamination of the acoustic signals due to integration of jet shear-layer hydrodynamic fluctuations. The downstream extension of the cone is however sufficient to recover the bypass duct radiation over the angular range of interest.

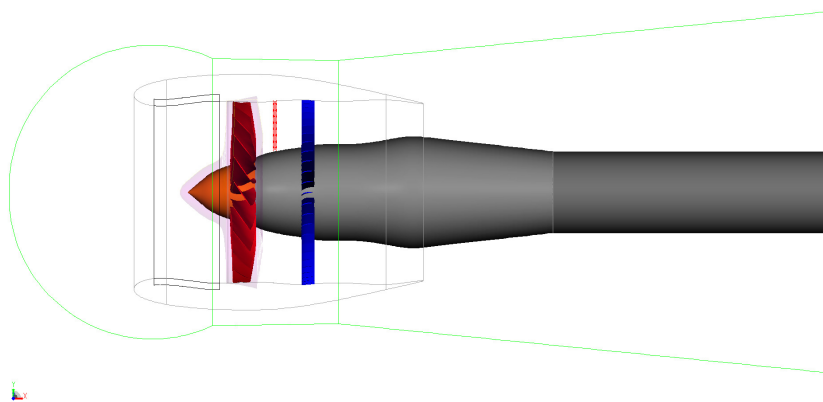


Figure 3. Computational setup.

Simulations have been performed by using four values of the mesh resolution. PowerFLOW generates automatically a Cartesian volume grid around a set of individual solid parts, starting from a value of the minimum hexahedral cell (voxel) size, a number of Variable Resolution (VR) levels, from the finest to the coarsest one, with changes of the voxel size between adjacent VRs by a factor of two, and the definition of the VR regions. The real surface of the body is recovered automatically by intersecting the Cartesian mesh with the solid parts and generating a collection of polygons (surfel).<sup>25,26</sup> Surfels are generated whenever a surface representation is necessary, for instance, in the definition of the boundary between a fixed volume mesh and

a rotating volume mesh around a rotor. The boundary conditions are prescribed on the surfels and not on the nodes of the Cartesian mesh, therefore, high accuracy is preserved in the representation of complex shapes and complex rotating mesh boundaries. The four values of the mesh resolution used in the present study are reported in Table 1, together with the corresponding number of voxels, Fine Equivalent Voxels (FEV) and Fine Equivalent Surfels (FES). The fine equivalent elements represent the number of elements weighted by the time stepping rate, which is proportional to the mesh resolution level<sup>b</sup>. The overall CPU cost for 10 rotor revolutions is also reported. Notice that, for the finest case, which represents our best CPU cost/accuracy trade-off for a case with resolved blade tip gap, the overall CPU cost is about 60 thousand hours, corresponding to a turnaround time of about 3.5 days with 720 cores.

Resolution	VRs	$\Delta(mm)$	Voxels	FEV ( $10^6$ )	FES ( $10^6$ )	CPU h ( $10^3$ )
coarse (no gap)	15	0.3660	300	85	25	2
medium (no gap)	15	0.2610	420	119	35	4
fine (untripped)	15	0.1830	600	171	49	30
extra fine (tripped)	16	0.0915	916	136	36	60

Table 1. Mesh resolution, number of mesh elements and CPU hours (Intel Xeon CPU E5-2680 2.80GHz CPU).

The coarse and medium resolution runs have been executed in a preliminary stage of the activity with the intent of performing a setup sanity check and a mesh resolution study in terms of aerodynamic performances. For these two runs the finest voxel size was not small enough to resolve the blade tip gap, which has been therefore removed by extending the blade radially and letting PowerFLOW managing the casing/blade overlapping. The axial momentum on the rotor, based on the rotor front surface, blade radius and tip velocity, is plotted in Fig. 4. The first coarse run has been executed for more than 45 rotor revolutions, but an adequate statistical convergence is reached after 10 rotor revolutions. The current best practice for this class of simulations is to perform a medium resolution run with gap over 10 rotor revolutions, and then use the last frame to seed a fine resolution run, which is executed with an initial settling time of few blade passage periods. The overall CPU cost per geometry is therefore about 90 thousand CPUh. The three coarser runs exhibit a clear mesh convergence trend. The extra fine mesh has been obtained by adding an additional VR region around the blade tip and around a trip on the rotor blade, as discussed hereafter. The reduction of the axial momentum by about 4% is due to a better resolution of the tip gap. The results reported in this work correspond to the fine untripped case (*untripped*), a fine untripped case, but with a twice finer mesh resolution in the interstage (*untripped fine*), a non recurrent run, not included in Table 1, and an extra fine tripped run (*tripped*). All these runs have the same VR mesh layout, with a voxel size of 0.366 mm past the rotor and stator blades.

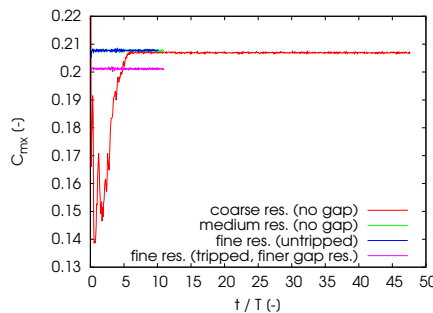
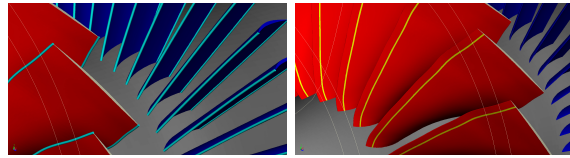


Figure 4. Rotor axial momentum coefficient for baseline SDT configuration and different mesh resolutions.

Due to the very small leading and trailing edge radii, a finest VR region has been defined around the edges through cylindrical volumes of 1 mm radius, as shown in Fig. 5. The trips on the rotor blades are also shown in the same figure. These are obtained by offset of a chord segment of 1.5 mm in the normal direction by a distance of 0.37 mm (about four voxel cells per trip height).

<sup>b</sup>The solution in a twice coarser voxel is updated with a twice larger  $\Delta t$  and is therefore two times cheaper.



**Figure 5.** Details of the computational setup: high mesh resolution regions around the blade edges (left), trip on the rotor blade (right).

## II.D. Time-average flow field

As a setup sanity check and adequacy of the mesh resolution in terms of aerodynamic performances, it is useful to compare the time-average flow solution with validated RANS results provided by NASA. Fig. 6 shows the time-average velocity fields in the symmetry plane for the baseline configuration. Notice that the stage region is not available in the RANS results. Outside the stage region, LB/VLES and RANS results are in good qualitative agreement, the main differences taking place in the secondary shear layer, where the PowerFLOW resolution is intentionally coarser than what required to resolve the turbulent mixing and thus the secondary jet noise, which is outside the present scope.

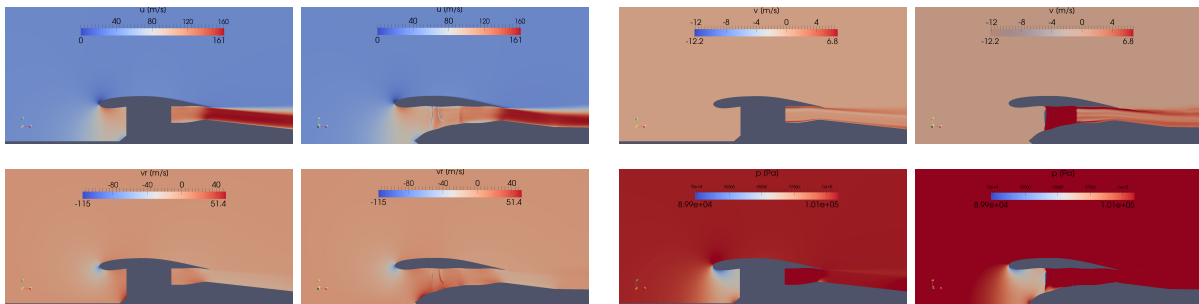


**Figure 6.** Time-average flow field on the symmetry plane. Comparison between NASA (left in each pair), and PowerFLOW results (right). Axial velocity (top, left), azimuthal velocity (top, right), radial velocity (bottom, left), and pressure (bottom, right). SI units.

The predicted mass flow rate is compared to the measured ones for the three SDT configurations in Table. 2. The discrepancy between measurements and simulations is around 1%, which is larger than the estimated experimental uncertainty based on the reported values by NASA<sup>27</sup> for the wind tunnel total pressure (51 Pa), and inlet Mach number (0.0004). However, the achieved aerodynamic prediction accuracy should result in acoustic prediction uncertainties smaller than the noise measurement uncertainties of about 1 dB.<sup>27</sup> In other words, discrepancies between measured and predicted noise levels are unlikely to be due to a lack of accuracy in the prediction of the time-average flow field.

Configuration	Measurements	Simulations	$\Delta$
Baseline (untripped)	26.54	26.25	1.09%
Baseline (tripped)	26.54	26.18	1.36%
Low-Noise (tripped)	26.44	26.27	0.83%
Low-Count (tripped)	26.54	26.27	1.02%

**Table 2.** Comparison between measured and predicted mass flow rate [kg / s] for the three SDT configurations.

## III. Interstage velocity field

### III.A. Phase-locked velocity maps

Phase-locked average velocity maps at station #1 for the baseline configuration are shown in Fig. 7. Hot-wire measurements are compared to three sets of numerical results with the intent of investigating the effect

of some setup modifications. The first set of results corresponds to untripped rotor blades. For reasons explained in the next paragraph, a second set of results was obtained by doubling the mesh resolution in the interstage region. Finally, a third set of results corresponds to a tripped rotor blade, the same resolution in the interstage region as for the first set of results, and a twice finer mesh resolution in the tip gap. The three set of numerical results do not exhibit significant differences and deviate from the measurements by less than about 10%. The axial component, in particular, is underestimated and exhibits a thicker boundary layer along the casing. The reason of this discrepancy, which is not consistent with the mass flow prediction accuracy, is not understood. An error is thus potentially affecting the stage total pressure, but this information is not currently available in the data set.

Corresponding root-mean-square (rms) velocity maps are also shown in Fig. 7. The three set of numerical results exhibit clear differences in two regions: close the casing and in the inner part of the rotor wake. A finer mesh resolution in the interstage results in significantly higher turbulent levels close to the casing, and only slightly higher levels in the wake. Conversely, adding the trip produces only slightly higher turbulent levels close to the casing and significantly higher levels in the wake, in particular, closer to blade root. Comparing these results to the hot-wire measurements reveals an overestimation of the turbulent levels close to the casing and in the outer radial part of the wake, as well as a more accurate prediction of the turbulent levels in the root wake region. Our opinion is that the presence of the trip in the simulation allows to mitigate the effects due to a lack of rotor blade resolution to resolve an intrinsically intermittent low Reynolds number flow. The trip is perhaps not necessary for higher rotor speeds, but this needs to be verified with a new simulation campaign extended to different operating conditions, including the transonic take-off one.

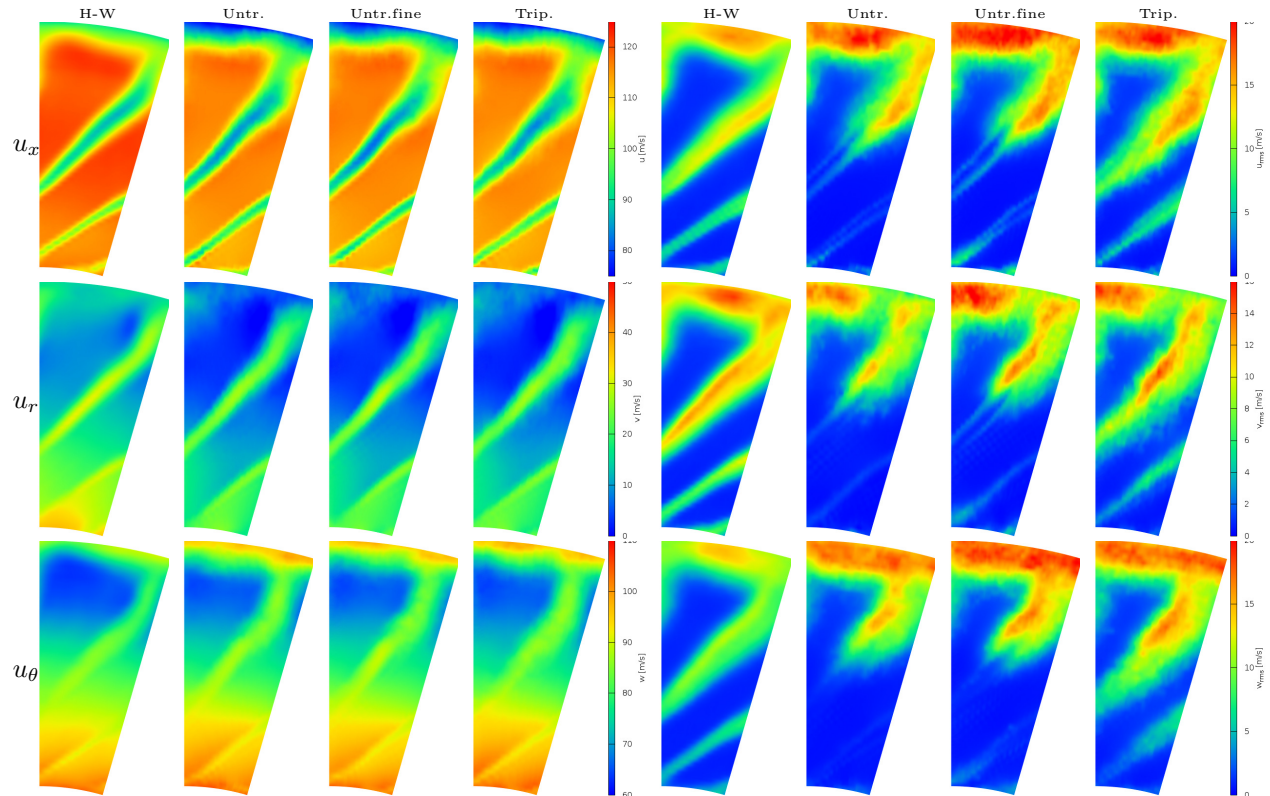


**Figure 7.** Phase-locked average (left block) and rms velocity (right block) at station #1 [m/s]. Axial, radial and azimuthal velocity in the top, middle and bottom rows, respectively. Hot-wire measurements on the left column, PowerFLOW results for untripped, untripped-fine and tripped cases from second to forth columns.

### III.B. Velocity spectra

Narrow-band spectra of the velocity fluctuations at three radial locations are shown in Figs. 8 through 10. The length of the signals corresponds to 110 and 10 rotor revolutions for the hot-wire measurements and sim-

ulations, respectively. For both data sets, Fourier transforms are computed with a bandwidth of 28.6293 Hz, 50% window overlap, and Hanning weighting. Fig. 8 shows results at one point very close to the casing. The three different PowerFLOW setups provide similar results and both the mesh resolution in the interstage region and the blade trips have a small but consistent effect, in particular, at frequencies higher than 4 – 5 BPF harmonic counts.

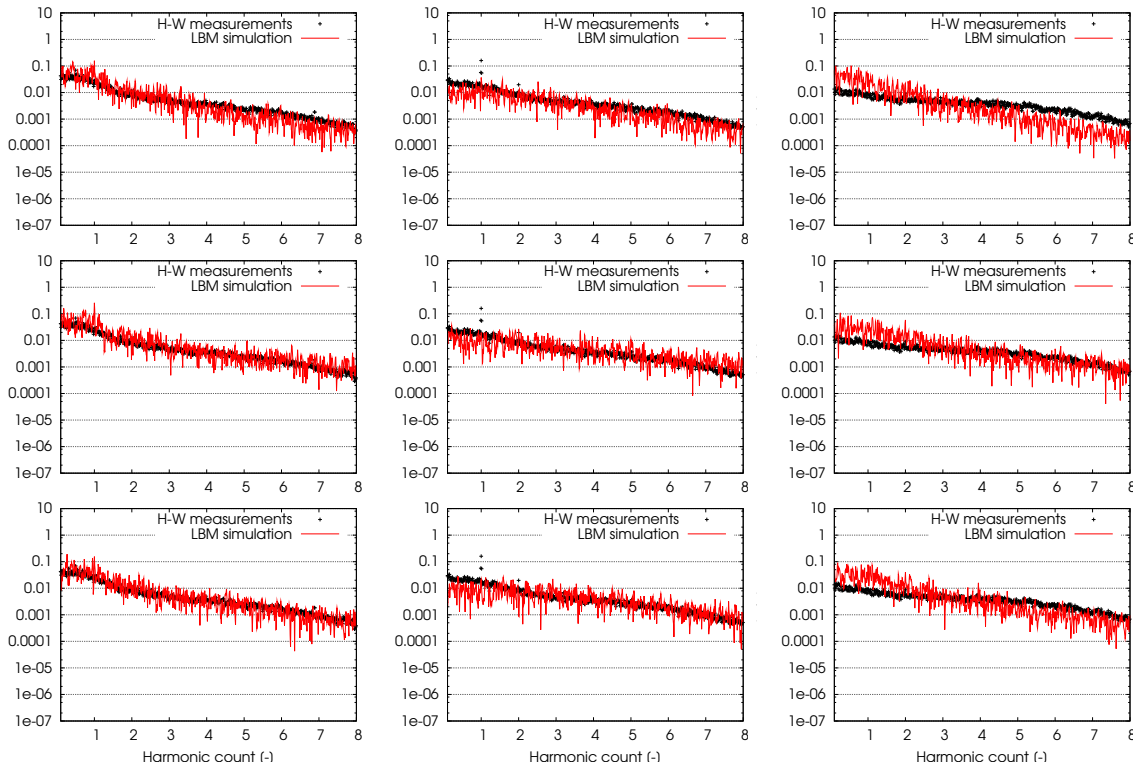


**Figure 8.** Velocity spectra at station #1 and  $r = 0.275997\text{ m}$ . Axial, radial and azimuthal velocity in the left, middle and right columns, respectively. Comparison between hot-wire measurements (symbols) and PowerFLOW results for untripped (top), untripped-fine (middle) and tripped (bottom) cases.

Spectra at 80% radial location are plotted in Fig. 9. Broadband results for the tripped case are in better agreement with the measurements than for the other cases. For all cases, the tonal levels of the radial and azimuthal components are, respectively, under- and overestimated.

Finally, spectra at 60% radial location are plotted in Fig. 10. At this location, only the broadband levels of the tripped case are in good agreement with the measurements, but only for axial and radial components, and only below a harmonic count of about 4. Beyond this frequency, the axial and radial velocity fluctuations are underestimated by almost one order of magnitude. The azimuthal velocity fluctuation for the tripped case is underestimated by about one order of magnitude beyond a harmonic count of 1. Fluctuation levels for the untripped and untripped-fine cases are underestimated by two/three orders of magnitude. These results are of course consistent with the rms velocity maps shown in Fig. 7. As already observed in Fig. 9, for all cases, the tonal levels of the radial and azimuthal components are, respectively, under- and overestimated.

#### IV. Far-field noise and source power level

Far-field noise results obtained by integration of the FW-H equation on the permeable surface plotted in Fig. 3 are presented in this section. Three sets of results are reported:

- narrow-band noise Power Spectral Density (PSD) spectra in dB/Hz at several angular locations on a circular array of 10 m radius, with a constant angular spacing of  $5^\circ$ , from  $30^\circ$  (front) to  $150^\circ$  (aft);
- Overall Sound Pressure Level (OASPL) in dB on a linear sideline array 2.25044 m away from the engine axis, with a constant angular spacing of  $5^\circ$  of the microphones, from  $30^\circ$  to  $140^\circ$ ;

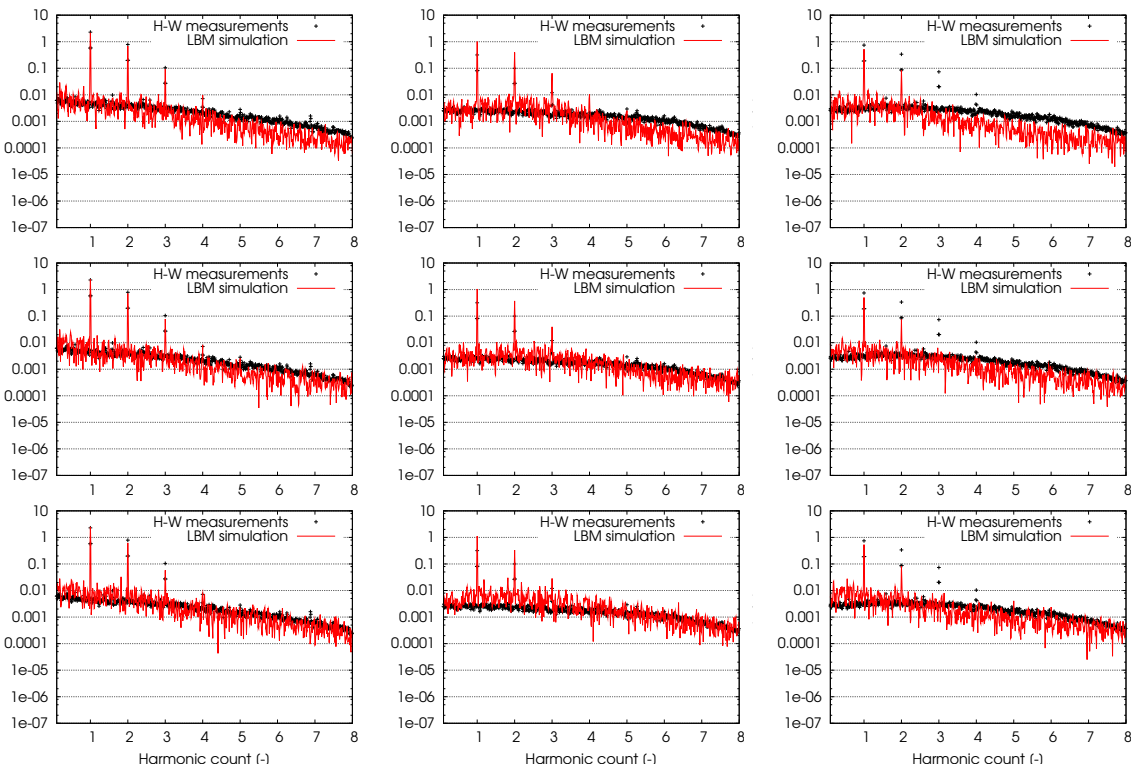


Figure 9. Velocity spectra at station #1 and  $r = 0.223292\text{ m}$ . Axial, radial and azimuthal velocity in the left, middle and right columns, respectively. Comparison between hot-wire measurements (symbols) and PowerFLOW results for untripped (top), untripped-fine (middle) and tripped (bottom) cases.

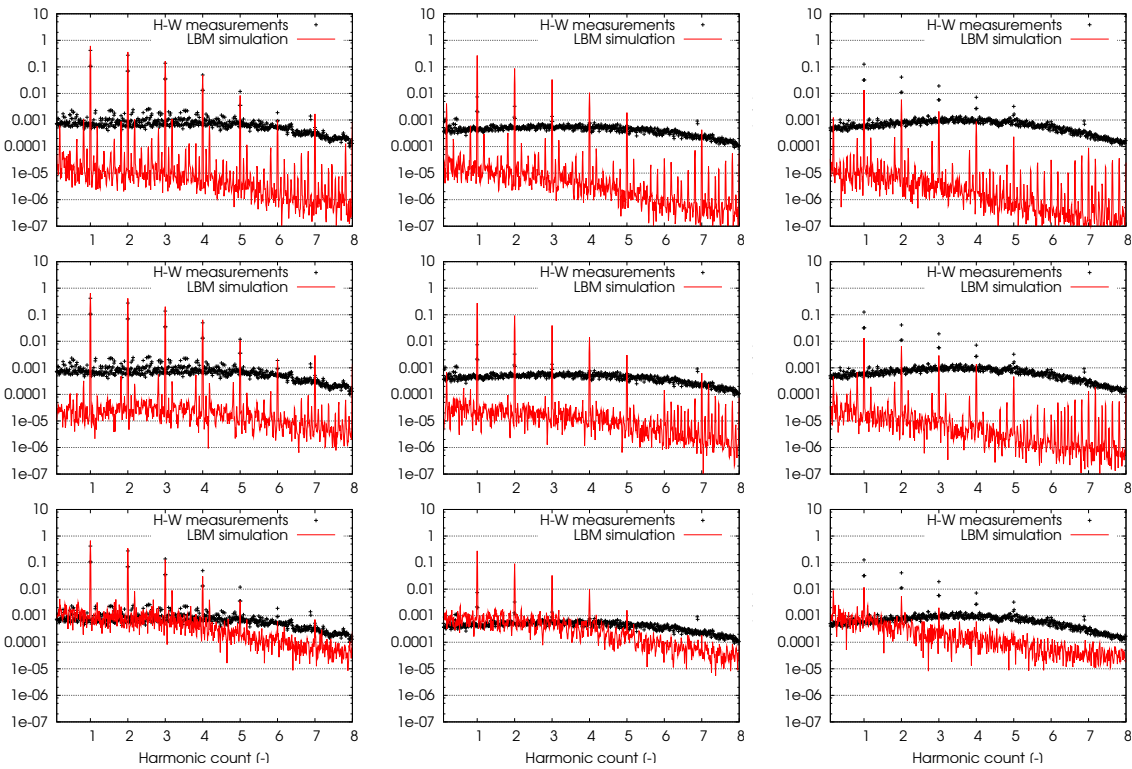


Figure 10. Velocity spectra at station #1 and  $r = 0.167640\text{ m}$ . Axial, radial and azimuthal velocity in the left, middle and right columns, respectively. Comparison between hot-wire measurements (symbols) and PowerFLOW results for untripped (top), untripped-fine (middle) and tripped (bottom) cases.

- narrow-band source Power Level (PWL) in dB/Hz, computed by integration of the acoustic intensity over the spherical surface portion corresponding to the aforementioned circular array, using the following formula:

$$\text{PWL}(f) = \int_{\theta_{\min}}^{\theta_{\max}} 2\pi R^2 \sin(\theta) \frac{[1 - M_\infty \cos(\theta)]^2 \text{PSD}(f, \theta)}{2\rho_\infty c_\infty} d\theta, \quad (1)$$

where  $R$  is the array radius,  $\theta$  is the radiation angle varying from  $\theta_{\min} = 30^\circ$  to  $\theta_{\max} = 150^\circ$ ,  $M_\infty$  is the free-stream Mach number, and  $\rho_\infty$  and  $c_\infty$  are the ambient density and speed of sound. The PSD is expressed in Pa<sup>2</sup>/Hz and the value of PWL is than converted in dB. The integration is performed using a Simpson formula. This expression of the power level does not account for the difference between emission and geometric angles that can be neglected at the present value of  $M_\infty$ .

All the results have been obtained by performing an azimuthal average of the signals computed at four azimuthal angles (every 90°). More precisely, signals cropped at an integer number of blade passage periods have been appended. Therefore, for every microphone location on both the linear and circular array, a signal duration of almost 40 rotor revolutions has been used. The Fourier transforms have been performed with a bandwidth of 28.6293 Hz and Hanning weighting.

Fig. 11 shows the effect of the computational setup for the baseline configuration on the noise spectra at two angular locations corresponding to the angles of maximum front and aft radiation. The effect of increasing the interstage mesh resolution and tripping the blade is higher at the aft microphone, and this is consistent with the fact that the main effect is to increase the wake/OGV interaction noise, which is prominently transmitted through the bypass duct. The overall setup effect on the aft radiated noise is a uniform shift of about 4 dB over the whole frequency range.

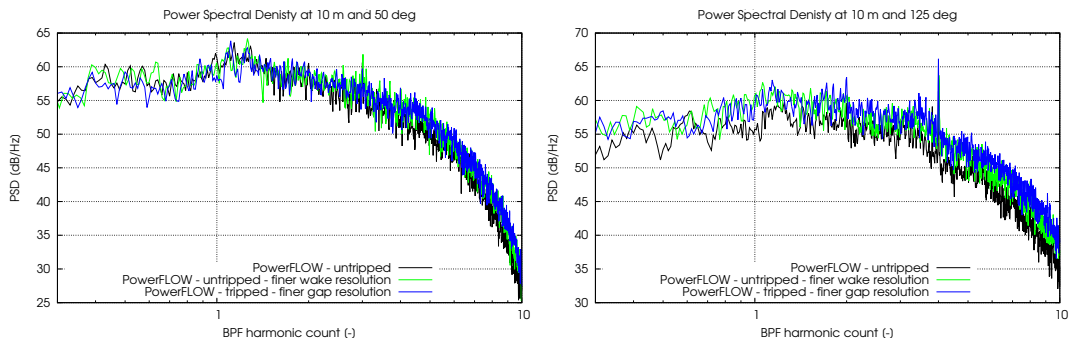


**Figure 11. Effect of computational setup on the far-field noise spectra at a distance of 10 m and angular location of 50° (left) and 125° (right).**

The OASPL levels along the linear array and the PWL spectrum are shown in Fig. 12. Tripping the blades allows to recover the right ratio between maximum front and aft radiation, thus resulting in a consistent discrepancy with the measurements of about 2 dB. The far-field noise measurement uncertainty is estimated to be of the order of 1 dB.<sup>27</sup> We are therefore committed to a further improvement of about 1 dB of our prediction<sup>c</sup>. Curiously, the PWL spectrum, although derived from the far-field PSD, does not show the same overestimation, but instead a broadband underestimation. However, since no tonal peaks appear in the experimental curve, we may argue that these have been artificially removed from the far-field noise measurements before computing the OASPL. This could explain the overestimation of the OASPL levels. The mesh cut-off frequency for the present simulation is expected to be about 15 kHz. Beyond this frequency, the progressive deviation of the prediction from the measurements is mostly due to the dissipation of the acoustic waves in the propagation from the fan/OGV to the FW-H surface. Consistently with the far-field OASPL levels, we can observe the expected trend between the three sets of numerical results, with the tripped results providing up to 4 dB higher values than the untripped case.

The effect of the different OGV configurations is now illustrated by comparing three sets of tripped blade results. Fig. 13 shows the OGV effect on the noise spectra at 30° and 125°. Both angular locations reveal

<sup>c</sup>The experimental OASPL data are not part of the FBN workshop, but have been extracted from Ref.<sup>28</sup> Our statement concerning the far-field noise prediction accuracy can therefore change if future official releases would deviate from the present data set.

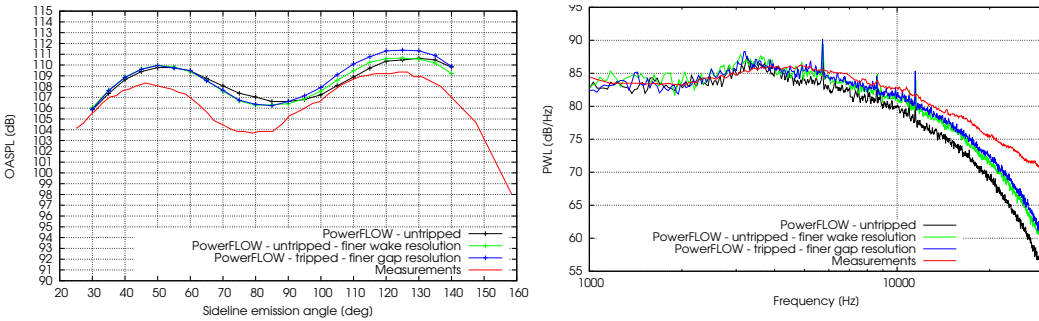


Figure 12. Effect of computational setup on far-field OASPL along the sideline array (left) and PWL (right).

that the low-noise and low-count OGVs generate lower broadband noise levels. However, the tonal content is very different. In the front microphone, for instance, the low-count OGV produces clear tones at the BPF-1, BPF-2 and BPF-4. For the other OGVs, the broadband levels overwhelm the tones, with the exception of BPF-3 for the baseline OGV. For all OGVs, some BPF-1 subharmonic components can be observed, which are likely to be due to the interaction between the rotor tip vortices and the blades. Because of the viscous effect of the wall, the tip gap vortices rotate at a lower speed than the blades. As a consequence, interactions with the rotor blades take place at a statistically smaller frequency than the rotational frequency<sup>d</sup>. The noise spectra at the aft microphone exhibit a clear noise reduction trend of the low-noise and low-count OGVs, starting from about 3 kHz. However, as for the front microphone, the tonal content is very different for the three configurations. A strong BPF-1 tone takes place for the low-noise and low-count OGVs, which emerges by 10 dB and 15 dB for the two configurations, respectively. The BPF-2 tone is very strong only for the low-count OGV, the BPF-4 tone takes place only for the baseline OGV and the BPF-5 only for the low-count OGV. The different tonal content is of course due to a different duct modal content in the engine, as discussed in Section V.

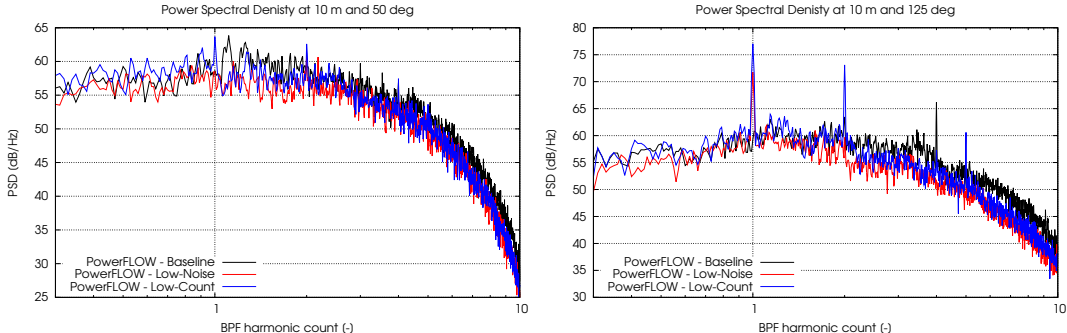


Figure 13. Effect of OGV configuration on the far-field noise spectra at a distance of 10 m and angular location of 50° (left) and 125° (right).

The OASPL levels along the linear array and the PWL spectrum for the three OGV configuration are shown in Fig. 14. Reference experimental PWL data are available only for the baseline OGV. Whereas, OASPL data, extracted from Ref.,<sup>28</sup> are available for the baseline and low-noise OGVs. All the effects observed in the far-field spectra can be observed also in these results. In particular, a clear broadband noise reduction trend associated with the lower OGV count, and a different tonal noise content. Interestingly, both low-count designs are louder than the baseline OGV at radiation angles larger than 130°–140°. This can be explained with the occurrence of duct modes in the bypass duct with a dominant shallow radiation attitude.

Finally, deltas of the OASPL between the baseline and the other configurations are plotted in Fig. 15. We have an experimental reference only for the low-noise design, which is very well captured by the numerical prediction, with discrepancies lower than 1 dB, which is equal to the experimental uncertainty.

<sup>d</sup>The tip/vortex interaction frequency would tend to zero if the tip vortices would rotate at the same speed as the fan.

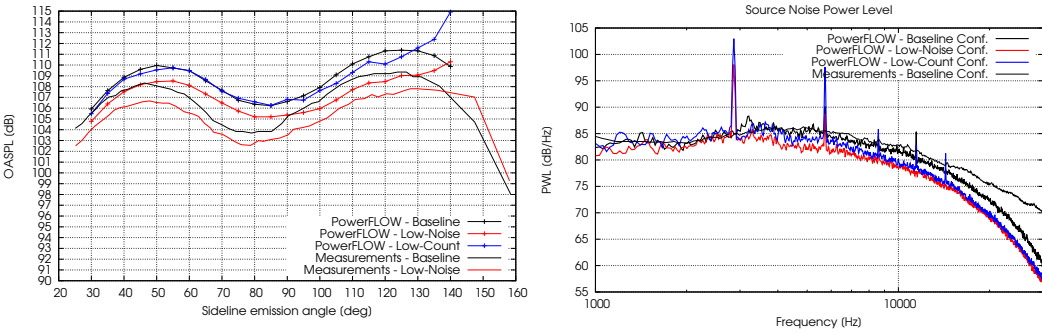


Figure 14. Effect of OGV configuration on far-field OASPL along the sideline array (left) and PWL (right).

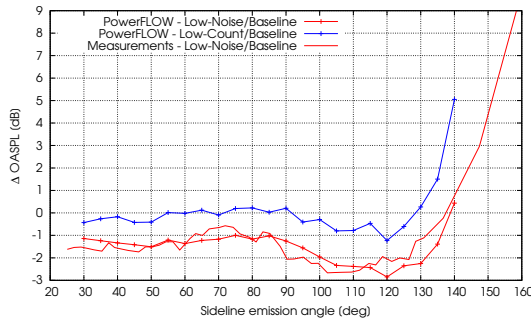


Figure 15. Effect of OGV configuration on far-field OASPL along the sideline array.

## V. Time/circumferential Fourier analysis and duct modal content

This section reports results of an azimuthal Fourier analysis carried out for the intake lip and bypass exhaust sections. For both time Fourier transforms have been computed with a bandwidth of 143.1465 Hz and by projecting the numerical solution on a uniform polar grid of 44 elements in the azimuth and 20 elements in the radial direction. Azimuthal modes in the range  $[-32 : 32]$  are shown. Duct modes are also extracted on these two sections, through a list square approach using a modal basis of 65 circumferential modes and 5 radial modes, with only cut-on modes retained in the basis. The modes are computed for the corresponding annular or hollow circular section and for an integral average Mach number. Upstream and downstream propagating modes are used for the intake lip and bypass exhaust sections, respectively. It should be mentioned, however, that the choice of these two sections, in particular the lip intake one, is not optimal in terms of infinite straight duct modal identification.

Circumferential Fourier modes and duct modes graphs corresponding to narrow bands components around the first and the second BPF are shown, for the baseline configuration, in Fig. 16. The rotor-locked component ( $m=22$ ) is clearly cut-off in the intake duct. The plane mode, which cannot be justified by any Tyler-Sofrin (T-S) combination, is non zero both in the intake and bypass ducts, and this can be due to a trapping mechanism involving the engine terminations, and/or the fan/OGV disks and, perhaps, a secondary jet column mode. Besides the rotor-locked component, all the circumferential modes at the first BPF cannot be justified by a T-S combination and are therefore due to a modal scattering mechanism involving multiple reflection on the rotor and the stator. The duct modes fitting reveals a rich radial mode content in the intake section, which can be indeed an artifact due to the location of the extraction plane. Conversely, the bypass exhaust section seems to be dominated by the first two radial modes. Interestingly, the power distribution across the modes in the intake duct exhibits a somehow increasing trend from negative to positive circumferential modes. The same trend is clearly visible for the second BPF. Moreover, the bypass section reveals the presence of strong  $m=-10$  mode, which results form a T-S combination ( $2 \times 22 - 1 \times 54$ ). The first four radial modes contribute to this circumferential mode.

Modes for the low-noise and low-count configurations are shown in Fig. 17 and Fig. 18 and exhibit very similar patterns. At BPF-1, the T-S modes  $-4, -30$  and  $22$  take place in the bypass duct. The mode  $m=-4$  is more than 10 dB higher than the others and can be clearly observed also in the intake duct. This



**Figure 16.** Circumferential Fourier mode decomposition (top) and cut-on duct modes fitting at the intake lip section (middle) and bypass exhaust section (bottom) for baseline configuration. BPF-1 (left) and BPF-2 (right) results.

is certainly the mode responsible for the far-field BPF-1 tone observed in Fig. 13. Due to its low order, this is a mode that tends to have a shallow radiation lobe and is therefore very likely the one responsible for the OASPL increase at high radiation angles observed in Fig. 14. The magnitude of this mode is about 2.5 dB higher for the low-count OGV than for the low-noise OGV, and this can partially explain why the low-count OGV is about 4 dB louder than the low-noise OGV at  $140^\circ$ . At BPF-2, the acoustic field is clearly dominated by two T-S modes:  $m=18$ , both in the intake and bypass ducts, and  $m=-8$  only in the bypass duct.

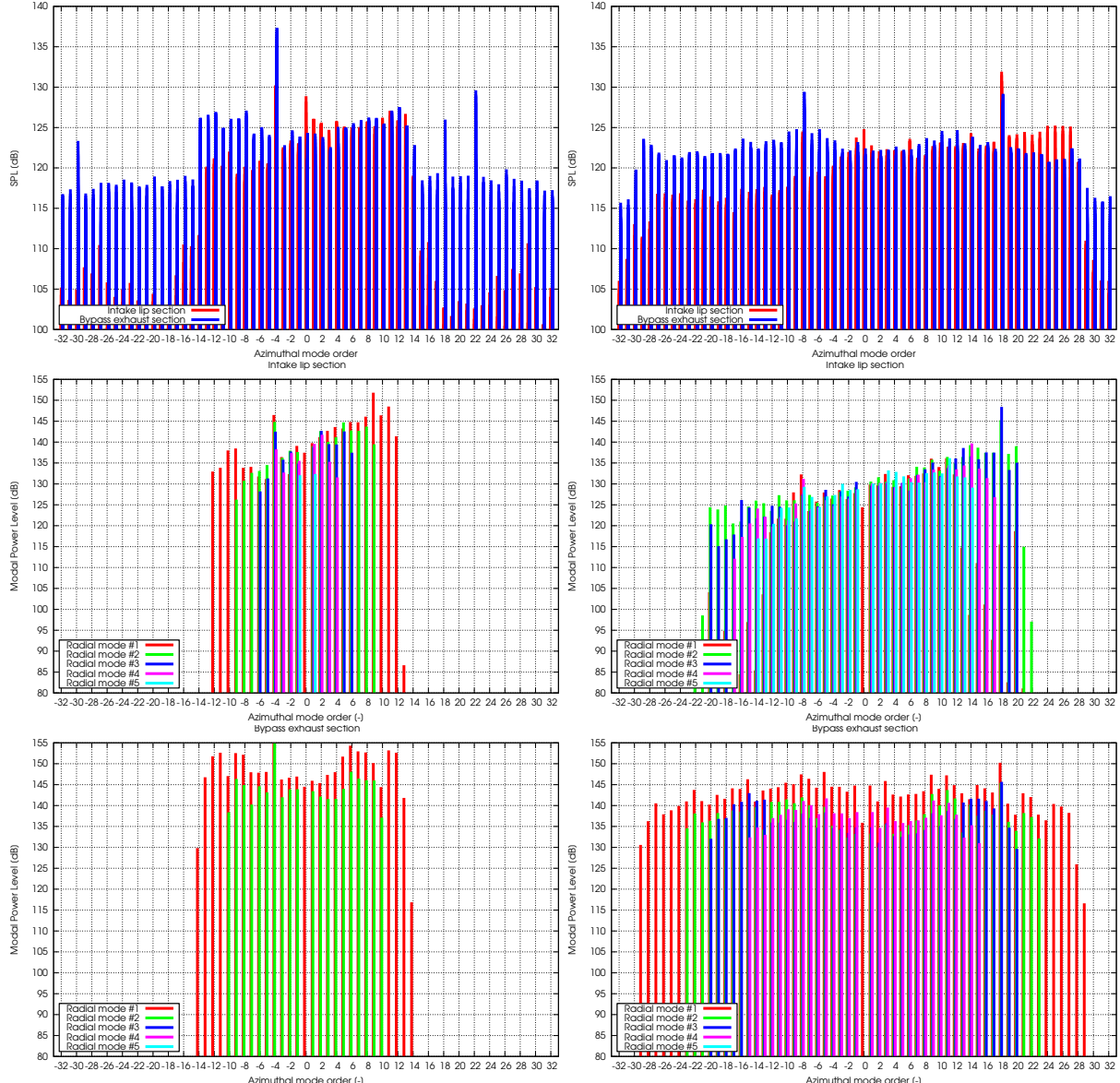


**Figure 17.** Circumferential Fourier mode decomposition (top) and cut-on duct modes fitting at the intake lip section (middle) and bypass exhaust section (bottom) for low-noise configuration. BPF-1 (left) and BPF-2 (right) results.

All the Fourier mode results reveal the importance of modal scattering mechanisms that contribute to enrich the duct mode content. This is clearly a broadband mechanism that can better visualized looking at a wider frequency range. Following the analysis of Ref.,<sup>11</sup> we performed time Fourier computations with a bandwidth of 715.7325 Hz, a quarter of BPF, and performed Fourier analyses, for every band, in the azimuthal range  $[-50 : 50]$ . A polar uniform mesh of 200 circumferential and 20 radial elements has been used. The results are represented as modal magnitude maps, for both the intake and the bypass sections, in Fig. 19. The boundary between cut-on and cut-off modes is visible, with a slight unsymmetrical pattern

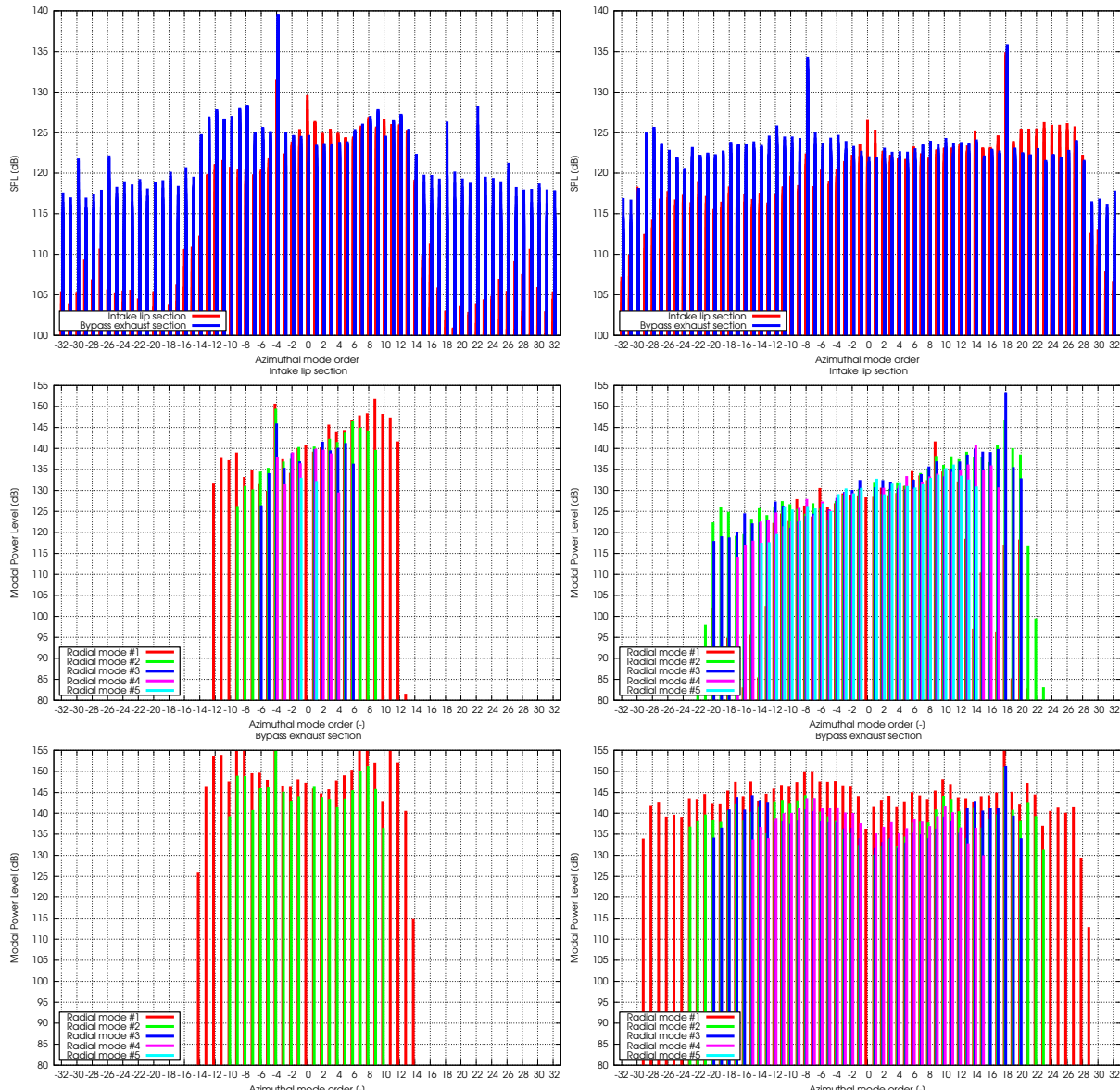


**Figure 18. Circumferential Fourier mode decomposition (top) and cut-on duct modes fitting at the intake lip section (middle) and bypass exhaust section (bottom) for low-count configuration. BPF-1 (left) and BPF-2 (right) results.**

between negative and positive modes, which is due to the convection effects. The positive modes exhibit slightly larger magnitude than their negative counterparts. Overall, the acoustic field is continuously broad in space and time and this constitutes a serious limit to the usage of frequency-domain approach in the framework of nacelle and liner designs. Based on this observation, we believe that the present time-domain LB/VLES technology constitutes the only viable and reliable solution for nacelle and liner design, since it is able to provide a full insight into the broadband modal content of an engine with a turnaround time that is in line with the industrial design cycles.

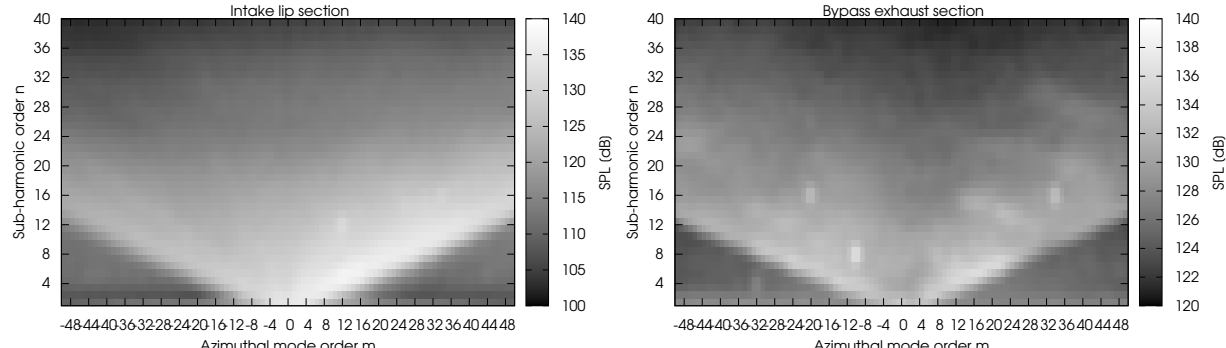


Figure 19. Time/circumferential Fourier component maps: intake lip section (left) and bypass exhaust section (right).

## VI. Effects of the honeycomb liner

### VI.A. Liner design

The SDT fan/OGV configuration was specifically designed with the intent of reducing the tonal noise levels and highlight the broadband noise content. The baseline configuration, in particular, does not reveal any emerging cut-on T-S mode at BPB-1, and only one mode in the bypass duct at BPF-2. The noise spectra at 125° shows peaks at BPF-2 and BPF-4. Although these are mostly connected with the noise transmission through and radiation from the bypass duct, we have decided to carry out a proof-of-concept direct liner simulation by adding a 1-DoF honeycomb liner in the intake duct only, and by tuning this liner to these two harmonics.

The geometrical parameters of a 1-DoF liner are the thickness of the micro-perforated sheet, the diameter of the orifices, the depth of the underlying honeycombs, and the cross sectional size of the honeycomb. In the current work, we adopted the approximation of considering one orifice only per honeycomb cell, located in the center, therefore the face sheet porosity, which represents the fraction of sheet volume occupied by the fluid, is explicitly related to the cross sectional side of the honeycomb cell.

An analytical model of the impedance of 1-DoF liners was derived from Crandall's work<sup>29</sup> by Melling.<sup>30</sup> It models the linear response of the perforated sheet with a mathematical formulation based on a Poiseuille flow inside a pipe excited by acoustic waves. This analytical model was used in the present study to drive an optimal search based on a genetic algorithm with the maximization of the absorption at BPF-1 and BPF-2 as a target. A single objective was used by attributing a higher weight to the absorption at BPF-2.

Table 3 shows the range of variation of the liner parameters as proposed by Motsinger & Kraft,<sup>31</sup> as well as the optimal values.

honeycomb parameter	range	optimal design
face sheet thickness	[0.5 : 2] mm	0.6 mm
orifice diameter	[0.8 : 1.6] mm	1.6 mm
cell diameter	[2.4 : 6.8] mm	6.7 mm
depth	[0 : 50] mm	32.6 mm
porosity	[10% : 50%]	5.1%

Table 3. 1-DoF honeycomb liner design parameters.

Mann *et al.*<sup>24</sup> have evaluated the feasibility of a direct LB/VLES simulation of honeycomb liners. Kundt's tube results for a 1-DoF, a 2-DoF and a bulk absorber were compared to analytical and semi-empirical results. Grid-converged solutions in good agreement with the theoretical solutions were achieved. The same approach has been used in the present study to verify the behavior of the optimal liner defined through the theoretical model. A Kundt's tube simulation has been therefore carried out by using the finest mesh resolution available in the tripped simulation setup (0.0915 mm).

The optimal liner is depicted in Fig. 20, together with a comparison between the simulated and the theoretical absorption curves. The first peak at about 0.5 BPF represents the Helmholtz-type resonance of the honeycomb, which can be approximated by  $f_{HR} = \sqrt{S/(l'V)} c_\infty / (2\pi)$ , where  $S$  is the area of a perforation,  $l'$  is the face sheet thickness incorporating an opening correction, and  $V$  is the volume of a honeycomb cell. The second resonance corresponds to a  $\lambda/2$  standing wave along the honeycomb depth, whereas the third peak is a harmonic of this standing wave. This is an approximated interpretation of the resonance modes, since the Helmholtz resonance and the standing wave resonances are coupled, which results in a frequency shift of the peaks. This explains why the second harmonic of the standing wave at BPF-2 is not at BPF-4. Locating the Helmholtz resonance at a frequency lower than BPF-1 could be useful to attenuate the subharmonic components due to the interaction between the rotor tip vortices and the blades. Despite the discrepancies at higher frequencies, which are mainly caused by the constraints on the diameter of the Kundt's tube to avoid the occurrence of non planar cut-one modes up to BPF-5, the current setup is considered adequate to a conceptual study.

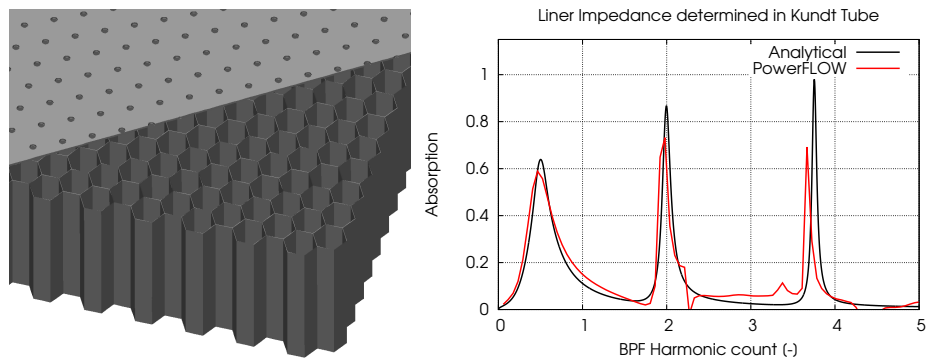


Figure 20. SDOF liner with the aim of high absorption at BPF-2: liner geometry (left) and its absorption (right).

By using a morphing procedure, the liner of Fig. 20 was transformed into an annular zero-splice liner and installed in the intake of the SDT baseline configuration, as illustrated in Fig. 1. The computational setup is derived from the baseline setup, by using the finest mesh resolution to fill the liner orifices. The number of FEV and the CPU time are 69% and 40% higher than for the baseline simulation, respectively.

## VI.B. Near-field effects and flow features

Fig. 21 shows the locations of three probes close to the intake liner, located at a distance of about 10 mm from the wall. For each probe, pressure spectra are computed for the baseline and the treated cases and compared by plotting the deltas of the corresponding narrow-band spectra. These results are in agreement with the absorption curve of Fig. 20. However, due to the properties of noise transmission through a duct, a reduction of the in-duct near-field pressure levels does not correspond to a similar far-field noise reduction.

Fig. 22 shows an instantaneous view of wall-normal velocity field in the honeycomb cells. A quite well established periodic pattern can be observed.

The honeycomb cells behave like Helmholtz resonators under grazing flow conditions. In order to visualize the liner behavior at the resonance frequencies, narrow-band Sound Pressure Levels (SPL) of the unsteady flow field in a plane through the honeycomb are computed and visualized in Fig. 23 for the Helmholtz resonance frequency, BPF-1, BPF-2 and BPF-4. As expected, standing wave patterns can be observed only for BPF-2 and BPF-4.

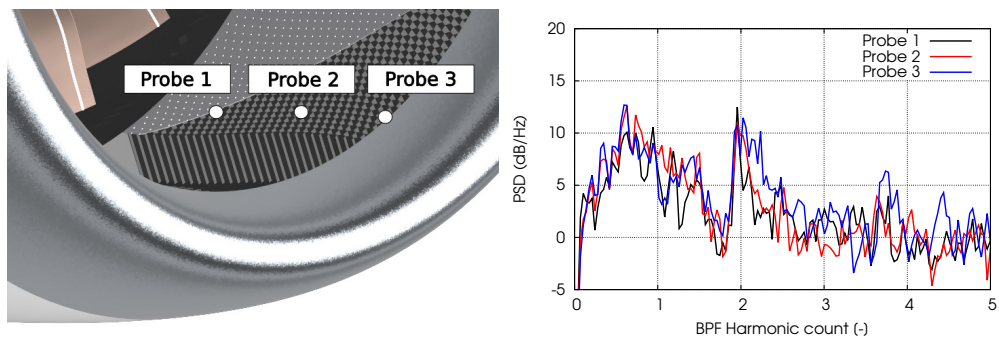


Figure 21. Near-field probes (left) and corresponding near-field narrow-band spectra (right) plotted as deltas between baseline and treated configuration results.

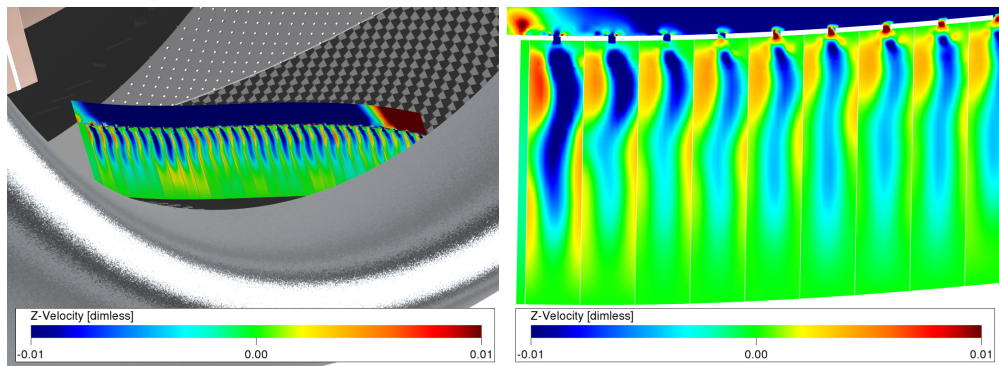


Figure 22. Wall-normal velocity normalized by the maximum velocity at the rotor tip in a plane cutting through the honeycomb.

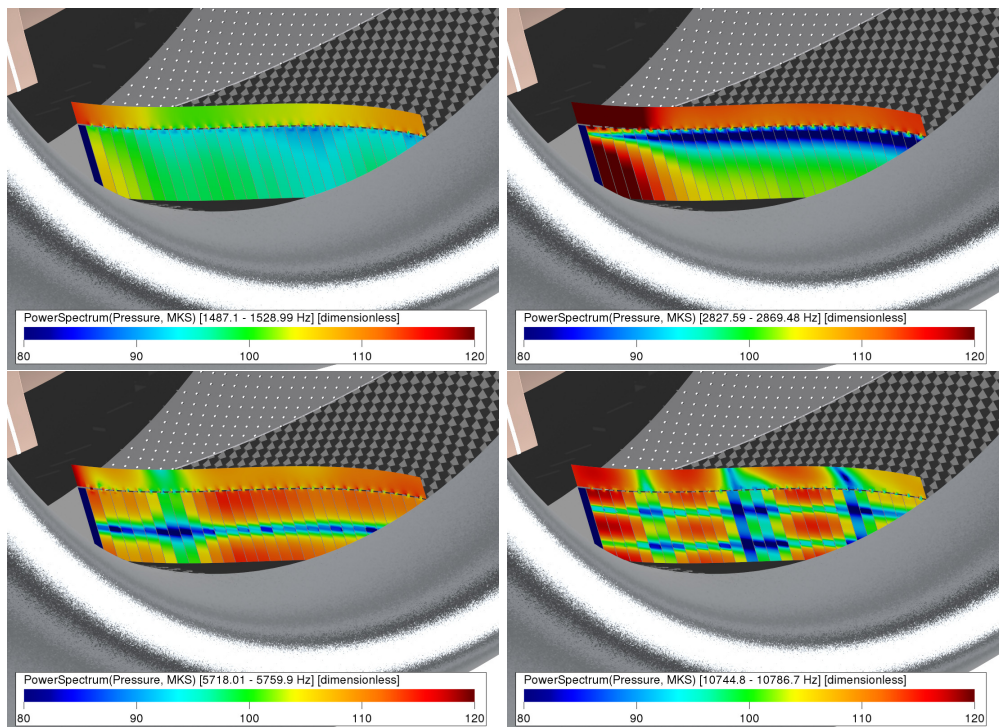
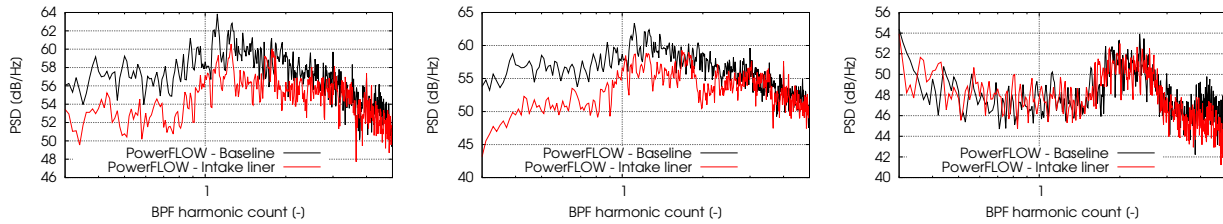


Figure 23. SPL field in plane cutting through the honeycomb computed in narrow bands around resonance frequencies: Helmholtz-resonance (top left), BPF-1 (top right), BPF-2 (bottom left), and BPF-4 (bottom right).

### VI.C. Far-field effects

The effects of the intake liner on the far-field noise levels are illustrated in this subsection. Noise spectra at a forward microphone location of  $50^\circ$  are plotted in Fig. 24 for the baseline and treated configurations. These spectra have been computed by integration on the whole FW-H surface of Fig. 3, the intake hemisphere only, and the exhaust cone only. As expected, the liner mitigates the far-field noise, but this is only due to a reduction of the intake contribution.



**Figure 24.** Effect of the intake liner on the far-field noise spectra at a distance of 10 m and an angle of  $50^\circ$ .

Finally, Fig. 25 shows the OASPL and the PWL spectrum for the baseline and treated simulations. A noise attenuation of about 2 dB in the forward radiation arc can be observed. Unfortunately, due to the absence of liner in the bypass duct, the tonal peaks in the PWL spectrum are almost unaffected by the presence of the liner, since these are radiated from the exhaust.

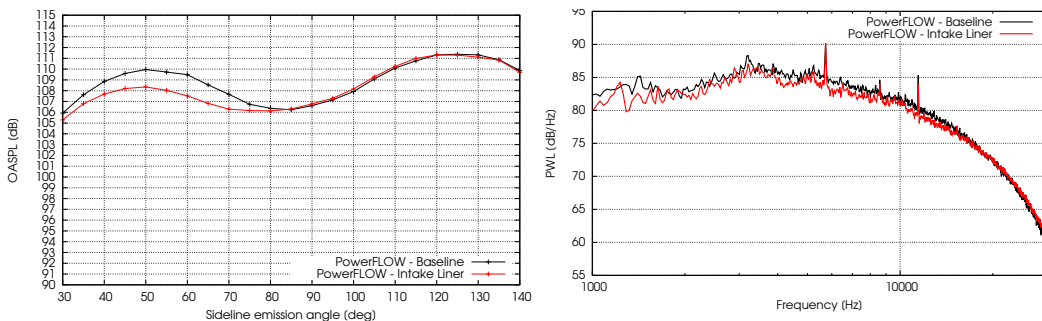


**Figure 25.** Effect of the intake liner on the far-field OASPL along the sideline array (left) and on the PWL spectrum (right).

## VII. Conclusions

The 22-in SDT fan/OGV experiment of NASA Glenn Research Center was repeated numerically using a LB/VLES simulations. Three OGV configurations and one rotational speed were considered, corresponding to an approach flight condition. Due to a combination of factors related to the expected transitional nature of the boundary layer on the rotor blades and to the mesh resolution, using a trip on the suction side of the rotor blade showed significant improvements of the prediction. Comparisons with available measurements revealed consistent trends between the three OGV configurations. In particular, based on previously published results by NASA, we pointed out an accuracy of the OASPL deltas between the baseline and the low-noise OGVs in less than 1 dB agreement with the measured deltas. Some of the findings for the low-noise and low-count configurations need to be confirmed by future data set releases by NASA. A time/circumferential Fourier analysis of the computed field clearly revealed the broadband nature in time and space of the flow and this is ultimately in favor of a time-domain approach for nacelle and liner optimization scopes. The computational turnaround time is of the order of one week per design on a 720-core cluster, and this is compatible with today industrial time constraints. Finally, we showed how a honeycomb liner can be incorporated in the flow simulation as an alternative to wall impedance modeling. Future efforts will be focused on the extension of the simulation matrix to the other operating conditions, including the transonic take-off one. Moreover, wall impedance models of the honeycomb liner will be tested and results will be compared to the present direct results.

## Acknowledgments

The authors wish to acknowledge Dr. Edmane Envia from NASA Glenn Research Center for providing the geometry and experimental data of the NASA 22-in fan source diagnostic test.

## References

- <sup>1</sup>Chen, H., Chen, S., and Matthaeus, W., "Recovery of the Navier-Stokes Equations Using a Lattice-Gas Boltzmann Method," *Physical Review A*, Vol. 45, No. 8, 1992, pp. 5339–5342.
- <sup>2</sup>Chen, H., Kandasamy, S., Orszag, S. A., Succi, S., and Yakhot, V., "Extended Boltzmann Kinetic Equation for Turbulent Flows," *Science*, Vol. 301, No. 5633, 2003, pp. 633–636.
- <sup>3</sup>Chen, H., Orszag, S., Staroselsky, I., and Succi, S., "Expanded Analogy Between Boltzmann Kinetic Theory of Fluid and Turbulence," *Journal of Fluid Mechanics*, Vol. 519, 2004, pp. 301–314.
- <sup>4</sup>Shan, X., Yuan, X.-F., and Chen, H., "Kinetic Theory Representation of Hydrodynamics: a Way Beyond the Navier-Stokes Equation," *Journal of Fluid Mechanics*, Vol. 550, 2006, pp. 413–441.
- <sup>5</sup>Glegg, S. A. L., "The Response of a Swept Blade Row to a Three-Dimensional Gust," *Journal of Sound and Vibration*, Vol. 227, Oct. 1999, pp. 29–64.
- <sup>6</sup>Posson, H., Moreau, S., and Roger, M., "On the Use of a Uniformly Valid Analytical Cascade Response Function for Fan Broadband Noise Predictions," *Journal of Sound and Vibration*, Vol. 329, 2010, pp. 3721–3743.
- <sup>7</sup>Ventres, C. S., Theobald, M. A., and Mark, W. D., "Turbofan Noise Generation, Volume 1: Analysis," *NASA Contractor Report CR-167952*, 1982.
- <sup>8</sup>Hanson, D. B., "Theory for Broadband Noise of Rotor and Stator Cascades with Inhomogeneous Inflow Turbulence Including Effects of Lean and Sweep," *NASA CR-2001-210762*, May 2001.
- <sup>9</sup>Posson, H., Moreau, S., and Roger, M., "On a Uniformly Valid Analytical Rectilinear Cascade Response Function," *Journal of Fluid Mechanics*, Vol. 663, 2010, pp. 22–52.
- <sup>10</sup>Posson, H., Moreau, S., and Roger, M., "Broadband Noise Prediction of Fan Outlet Guide Vane Using a Cascade Response Function," *Journal of Sound and Vibration*, Vol. 330, 2011, pp. 6153–6183.
- <sup>11</sup>Posson, H. and Moreau, S., "Effect of Rotor Shielding on Fan-Outlet Guide Vanes Broadband Noise Prediction," *AIAA Journal*, Vol. 51, No. 7, 2013, pp. 1576–1592.
- <sup>12</sup>Cooper, A. J. and Peake, N., "Trapped Acoustic Modes in Aeroengine Intakes with Swirling Flows," *Journal of Fluid Mechanics*, Vol. 419, 2000, pp. 151–175.
- <sup>13</sup>Hanson, D. B., "Mode Trapping in Coupled 2D Cascades - Aerodynamic and Ccoustic Results," *AIAA Paper 1993-4417*, 1993.
- <sup>14</sup>Premo, J. and Joppa, P., "Fan Noise Source Diagnostic Test - Wall Measured Circumferential Array Mode Results," *AIAA Paper 2002-2429*, 2002.
- <sup>15</sup>Nallasamy, M. and Envia, E., "Computation of Rotor Wake Turbulence Noise," *Journal of Sound and Vibration*, Vol. 282, 2005, pp. 649–678.
- <sup>16</sup>Mann, A., Pérot, F., Kim, M.-S., Casalino, D., and Fares, E., "Advanced Noise Control Fan Direct Aeroacoustics Predictions using a Lattice-Boltzmann Method," *AIAA Paper 2012-2287*, June 2012.
- <sup>17</sup>Sutliff, D. L., "Rotating Rake Turbofan Duct Mode Measurement System," *NASA TM-2005-213828*, 2005.
- <sup>18</sup>Pérot, F., Mann, A., Kim, M.-S., , and Casalino, E. F. D., "Investigation of inflow condition effects on the ANCF aeroacoustics radiation using LBM," *InterNoise, New York*, 2012.
- <sup>19</sup>Casalino, D., Ribeiro, A. F. P., Fares, E., Nöltig, S., Mann, A., Pérot, F., Li, Y., Lew, P.-T., Sun, C., Gopalakrishnan, P., Zhang, R., Chen, H., and Habibi, K., "Towards Lattice-Boltzmann Prediction of Turbofan Engine Noise," *AIAA Paper 2014-3101*, 2014.
- <sup>20</sup>Sanjose, M., Daroukh, M., Magnet, W., laborderie, J. D., Moreau, S., and Mann, A., "Tonal Fan Noise Prediction and Validation on the ANCF Configuration," *Proceedings of the International Conference on Fan Noise, Technology and Numerical Methods, 15-17 April 2015, Lyon, France*, 2015.
- <sup>21</sup>Woodward, R. P., Hughes, C., Jeracki, R., and Miller, C., "Fan Noise Source Diagnostic Test-Farfield Acoustic Results," *AIAA Paper 2002-2427*, 2002.
- <sup>22</sup>Envia, E., "Fan Noise Source Diagnostic Test-Vane Unsteady Pressure Results," *AIAA Paper 2002-2430*, 2002.
- <sup>23</sup>Pérot, F., Freed, D. M., and Mann, A., "Acoustic Absorption of Porous Materials Using LBM," *AIAA Paper 2013-2070*, May 2013.
- <sup>24</sup>Mann, A., Pérot, F., Kim, M.-S., and Casalino, D., "Characterization of Acoustic Liners Absorption using a Lattice-Boltzmann Method," *AIAA Paper 2013-2271*, May 2013.
- <sup>25</sup>Chen, H., Teixeira, C. M., and Molvig, K., "Digital physics approach to computational fluid dynamics: some basic theoretical features," *International Journal of Modern Physics C*, Vol. 8, No. 4, 1997, pp. 675–684.
- <sup>26</sup>Chen, H., Teixeira, C., and Molvig, K., "Realization of Fluid Boundary Conditions via Discrete Boltzmann Dynamics," *International Journal of Modern Physics C*, Vol. 9, No. 8, 1998, pp. 1281–1292.
- <sup>27</sup>Envia, E., Tweedt, D. L., Woodward, R. P., Elliot, D. M., Fite, E., Hughes, C. H., Podboy, G. C., and Sutliff, D. L., "An Assessment of Current Fan Noise Prediction Capabilities," *NASA TM 2008-2154115*, 2008.
- <sup>28</sup>Woodward, R. P., "Comparison of Far-Field Noise for Three Significantly Different Model Turbofans," *AIAA Paper 2008-49*, 2008.
- <sup>29</sup>Crandall, I. B., *Theory of Vibrating Systems and Sound*, D. Van Nostrand Company, New York, 1926.
- <sup>30</sup>Melling, T. H., "The Acoustic Impedance of Perforates at Medium and High Sound Pressure Levels," *Journal of Sound and Vibration*, Vol. 29, No. 8, 1973, pp. 1–65.
- <sup>31</sup>Motsinger, R. E. and Kraft, R. E., "Design and Performance of Duct Acoustic Treatment," *Aeroacoustics of Flight Vehicles: Theory and Practice, Volume 2: Noise Control*, edited by H. F. Nelson, NASA, Hampton, VA, 1991, pp. 165–206.